https://doi.org/10.1016/j.jsv.2018.11.013

This is the Pre-Published Version.

Tunable parallel barriers using Helmholtz resonator

Z. B. Wang and Y. S. Choy[a]

Department of Mechanical Engineering,

The Hong Kong Polytechnic University,

Hung Hom, Kowloon, Hong Kong SAR, China

[a]Corresponding author email: mmyschoy@polyu.edu.hk

© 2018. This manuscript version is made available under the CC-BY-NC-ND 4.0 license http://creativecommons.org/licenses/by-nc-nd/4.0/

Abstract

Parallel barriers are widely adopted to control environmental noise, but their performance may be inferior to that of a single barrier owing to the formation of multiple reflection waves between the parallel barriers. To improve the performance of parallel barriers, single or multiple Helmholtz resonators (HRs) are proposed to be mounted on the barrier surface. An acoustic interaction occurs between the HR and open cavity formed by the rigid ground and a pair of barriers, whereby the acoustic modal response within the open cavity is significantly suppressed and the diffraction wave at the barrier top edge is reduced. A semi-analytical model for dealing with acoustic coupling between the open cavity and HRs in a two-dimensional configuration is established in order to understand the sound suppression mechanism within the shadow zone. This model is also helpful for generating a noise control strategy that involves varying the dominant modal response at the target frequency. With the optimal position of a single HR, the insertion loss of about 10 dB around the target frequency can be controlled, while less influence is exerted on the off-target frequency. Comparisons are conducted between the data predicted using the present model and the numerical results obtained using the boundary element method, and the agreement between them is observed. Furthermore, experimental results demonstrate that the use of HRs for reducing noise in the shadow zone is feasible.

1. Introduction

A sound barrier is the most commonly used solution for environmental noise problems, and its applications can be extensively observed in both transport and industry. In general, a sound barrier is placed between the noise source and receiver to prevent the sound wave from approaching the receiver directly. In order to reduce the sound pressure level (SPL) on both sides of the road, parallel barriers are constructed face to face along the roadsides. However, their performance deteriorates owing to the multiple reflections between barriers, which forms a reverberant sound field within the boundaries [1-3]. Therefore, resonance forms in such unbaffled open cavity system, and multiple sound peaks can be observed at the receivers. In order to improve the performance, barriers with different edge profiles, such as circular, T-shaped, Y-shaped, arrow, and branched profiles have been designed, and their performances evaluated [4-6]. Among these, the T-shaped barrier provides the highest insertion loss, but it is generally not effective at low frequencies. To enhance the T-shaped barrier performance, a series of wells with a uniform depth or two different depths are aligned on the top of the barrier [7]. A slight improvement at low frequencies has been determined when the well depth is tuned appropriately. Moreover, wells with depths in a quadratic residue sequence, namely the quadratic residue diffuser (QRD), have been adopted to enhance scattering and sound absorption [8]. However, this system is probably bulky at the top edge of the barrier for low frequencies. In this regard, certain researchers have suggested the design of a sloped median barrier with different angles to redirect sound waves upwards, which diminishes the diffraction at the barrier top, thereby improving the barrier efficiency [9]. Similar to this mechanism, Pan et al. [10] recently proposed a wave trapping barrier (WTB), which is composed of a series of wedges in the shape of a trapezoid or triangular box, in order to redirect the sound reflection waves downwards to the ground so that the waves are trapped within the domain bounded by the two barriers [2]. Moreover, the wedge profile influences the sound pressure redistribution and resonance features, thereby modifying the diffraction strength at the barrier top. Alternatively, the barrier wall could be mounted with an array of small and hollow narrow tubes of different lengths to create a phase gradient and inhomogeneous impedance at the inner surface of the barriers to shield the sound waves inside the barriers. The inhomogeneous impedance slightly alters the acoustic trapped mode between the barriers and leads to improved noise reduction at the receiver [11].

Using the principle of alternating the acoustic mode inside the barriers, the Helmholtz resonator (HR) is proposed to be mounted on the barrier surface, which will undergo acoustic coupling between the open cavity and resonator, significantly changing the sound field between parallel barriers. In addition to this, the sound diffraction at the barrier top edge is expected to change. The HR is a common resonance control device that has been extensively used in ducts and enclosure systems. A series of work by the team of Cheng [12-15] systematically investigated the acoustic interaction between an enclosure and HRs. In order to widen the noise reduction frequency range inside the enclosure, multiple resonators with different resonance frequencies can be adopted [14]. A HR array can also be flush mounted on the duct wall to achieve a wide stopband and high transmission loss in silencer design [16-18] or a large cylindrical shell for controlling broadband sound transmission [19-21]. However, very little attention has been devoted to the acoustic coupling between the HR and open cavity or parallel barriers. Moreover, it is difficult to use conventional analytical and empirical methods to deal with such complex configurations. In the study of open cavities, numerous researchers have focused on investigating of the resonant phenomenon or acoustic mode inside the open cavities [22-24], but the relationship between the sound radiation and acoustic modal response in the open cavity has rarely been studied. Recently, Yang et al. [2] adopted the modal superposition method to calculate the SPL at the receiver behind the parallel barriers in order to understand the acoustic modal contributions. However, the SPL agreement between his method and boundary element method (BEM) can only be identified at resonance frequencies. The disagreement is probably a result of the non-orthogonality and incompleteness of the resonance modes in the open cavity [2, 25]. In this regard, Tong, et al. [25] proposed the use of frequency-dependent eigensolutions to construct the sound field inside and outside the open cavity. By considering acoustic coupling between the cavity and a semi-infinite space, different sets of eigensolutions or modal solutions can be obtained at different source frequencies. As a result, the SPL at different frequencies exhibits strong agreement with the numerical solutions obtained by the finite element method (FEM). This method motivates an important step forward in solving the acoustic coupling between the HR and two-dimensional open cavity in the current study. Therefore, the objectives of this study are: (1) to study the model that takes into account the acoustic coupling between the HR, open cavity with semi-infinite space in a two-dimensional configuration, theoretically and numerically; (2) to understand the mechanism of controlling the acoustic modal response in the open cavity by means of the HR and investigate its impact on the sound diffraction and suppression behind the barriers; and (3) to propose guidelines towards improved HR design for the mitigation of environmental noise.

The remainder of this paper is organized as follows. Section 2 outlines the theoretical model for the acoustic coupling between the parallel barriers and the HR array. A solution method is established to solve the fully coupled system among the HR, open cavity, and infinite exterior field. Modal analysis is carried out in section 3. An optimization process is conducted to search for the optimal resonator location so that superior performance can be obtained. Experimental validation is provided in section 4.

2. Formulation

Fig. 1 illustrates a model of two identical barriers erected on the ground, with the assumption of unchanged cross-section in the *z*-direction. The height and distance between the two barriers are denoted by L_y and L_x respectively. The coordinate origin is at the top-left barrier vertex. Two HRs are mounted on the barrier walls and the resonator aperture faces the space between the two vertical walls. The ground and the barrier walls are acoustically rigid, with the exception of the resonator opening. The entire space of the parallel barriers with the open region is divided into the cavity space Ω_a and upper-half semi-infinite space Ω_b. These are connected through the cavity opening with area S_{op}. A harmonic time dependence sound pressure in the cavity excited by a point source at $\vec{x}_s = (x_s, y_s)$ can be obtained by the two-dimensional inhomogeneous Helmholtz equation:

$$\nabla^2 p_a(\vec{x}) + k^2 p_a(\vec{x}) = -i\rho k c_0 q_s \delta(\vec{x} - \vec{x}_s), \tag{1}$$

where $k = \omega / c_0$ is the wavenumber, c_0 is the speed of sound, and $i\rho k c_0 q_s$ and $\vec{x}_s$ are the source strength and location, respectively, while p_a, with subscript *a*, indicates the sound pressure in space Ω_a. According to the momentum equilibrium at the interface of opening, we have

$$\frac{\partial p_a}{\partial n} = -i\rho k c_0 v_n, \tag{2}$$

where v_n is the particle velocity at the cavity opening.

The boundary condition for the acoustic resonator is

$$\frac{\partial p_a}{\partial n} = -i\rho k c_0 \frac{p_a}{Z_t^R}, \tag{3}$$

here, Z_t^R is the acoustic impedance of the *t*-th resonator.

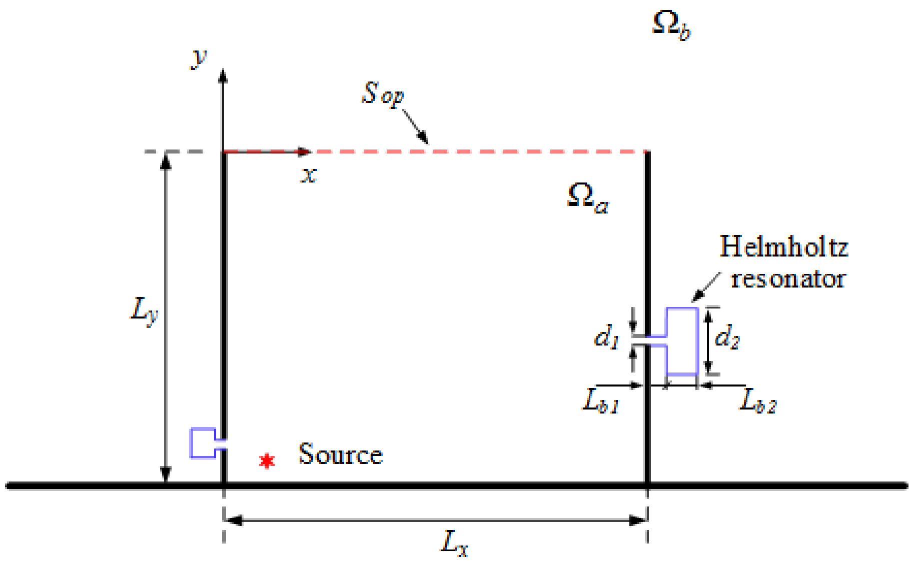

Fig. 1. A schematic diagram of the parallel barriers integrated with multiple Helmholtz resonators.

The acoustic pressure within the cavity is expanded as the superposition of the closed-cavity modal function, which has a complete and orthogonal feature:

$$p_a(\vec{x}) = \sum_{j=1}^{N} a_j \phi_j(\vec{x}), \tag{4}$$

where a_j is the modal response of the j-th eigenmode $\phi_j(\vec{x})$, and N is the maximum number of the truncated mode series. Furthermore, $\phi_j(\vec{x})$ is calculated by

$$\begin{aligned}\phi_j(\vec{x}) &= \psi_{j_x}(x)\cdot\psi_{j_y}(y) \\ &= \sqrt{\left(2-\delta_{0,j_x}\right)/L_x}\cos\left(j_x\pi x/L_x\right)\cdot\sqrt{\left(2-\delta_{0,j_y}\right)/L_y}\cos\left(j_y\pi y/L_y\right)\end{aligned}, \tag{5}$$

where $\delta_{i,j}$ is the Kronecker delta function, and the corresponding wavenumber of $\phi_j(\vec{x})$ is obtained by

$$k_j^2 = \left(j_x\pi/L_x\right)^2 + \left(j_y\pi/L_y\right)^2. \tag{6}$$

The sound pressure p_b in the space Ω_b is dominated by the sound radiation from the cavity opening S_{op}. By considering the Kirchhoff-Helmholtz integral equation, p_b at the receiver $\vec{x}$ is expressed as follows:

$$p_b(\vec{x}) = \int_s \left\{ G(\vec{x},\vec{x}_s)\frac{\partial p(\vec{x}_s)}{\partial n} - p(\vec{x}_s)\frac{\partial G(\vec{x},\vec{x}_s)}{\partial n} \right\} d\boldsymbol{s}, \tag{7}$$

where $G(\vec{x},\vec{x}_s)$ is the Green's function, $\vec{x}$ and $\vec{x}_s$ are the receiver point $\vec{x}$ in the space Ω_b and source point on the plane ***s***, respectively.

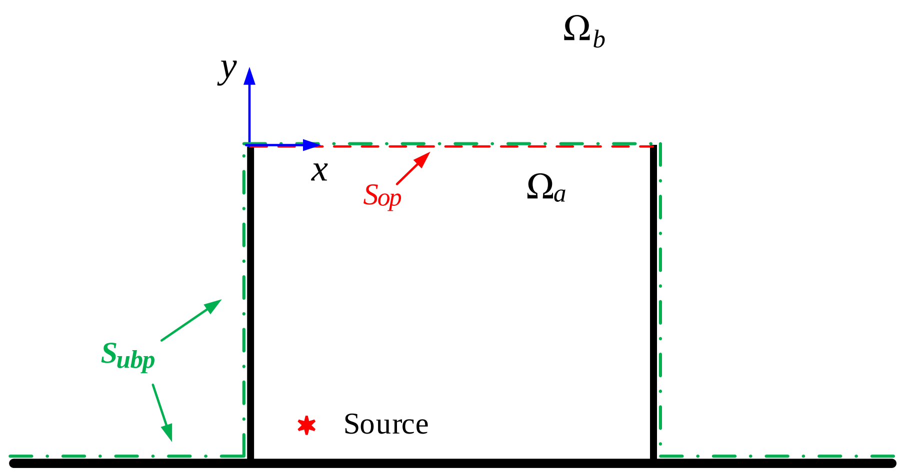

Fig. 2. Sketch of the integration surface used in Eq.(7) for the parallel barrier.

In this study, parallel barrier is formed by placing two thin rigid walls on an infinite surface. The integration at the right hand side of Eq.(7) is over the unbaffled plane, S_{ubp} which is indicated by the dash-dotted line in Fig. 2, including the infinite rigid ground surface, the thin walls and the cavity opening. Here, a Green's function satisfying the Neumann boundary condition at the unbaffled plane S_{ubp} is to be used so that the integration over the infinite rigid ground surface and two thin walls are eliminated. The Green's function which is denoted by G_{ubp} , is assumed to satisfy

$$\nabla^2 G_{ubp}\left(\vec{x},\vec{x}_{s_{ubp}}\right) + k^2 G_{ubp}\left(\vec{x},\vec{x}_{s_{ubp}}\right) = -\delta\left(\vec{x}-\vec{x}_{s_{ubp}}\right), \tag{8}$$

$$\frac{\partial}{\partial n} G_{ubp}\left(\vec{x}, \vec{x}_{S_{ubp}}\right) = 0, \qquad for \begin{cases} y = -L_y, & -\infty < x < 0 \\ y = 0, & 0 \le x \le L_x \\ y = -L_y, & L_x < x < \infty \end{cases} . \tag{9}$$

As a result, the second term on the right-hand side of Eq. (7) vanishes and Eq. (7) can be simplified as:

$$p_b\left(\vec{x}\right) = i\rho k c_0 \int_{S_{op}} G_{ubp}\left(\vec{x}, \vec{x}_{op}\right) \cdot v_n dS_{op} . \tag{10}$$

Moreover, the normal particle velocity v_n is expressed as a combination of the vibration modes such that

$$v_n = \sum_{m=1}^{M} b_m \psi_m\left(x_{op}\right) . \tag{11}$$

Substituting Eq.(11) into Eq.(10), the sound pressure p_b in the outside domain Ω_b can be rewritten as

$$p_b\left(\vec{x}\right) = \sum_{m=1}^{M} b_m \varphi_m\left(\vec{x}\right) , \tag{12}$$

in which

$$\varphi_m\left(\vec{x}\right) = i\rho k c_0 \int_{S_{op}} G_{ubp}\left(\vec{x}, \vec{x}_{op}\right) \cdot \psi_m\left(\vec{x}_{op}\right) dS_{op} . \tag{13}$$

Eq.(13) indicates that Green's function is used to obtain the value of $\varphi_m\left(\vec{x}\right)$. However, the unbaffled Green's function $G_{ubp}\left(\vec{x}, \vec{x}_{op}\right)$ cannot be expressed analytically and found numerically. To deal with this, the numerical tool of finite element method (FEM) is used to obtain $\varphi_m\left(\vec{x}\right)$ instead of finding $G_{ubp}\left(\vec{x}, \vec{x}_{op}\right)$. Details of using the finite element method to attain $\varphi_m\left(\vec{x}\right)$ is described in section 3.1.

The sound fields at the two domains are coupled based on the continuity condition $p_a\left(\vec{x}\right)\big|_{S_{op}} = p_b\left(\vec{x}\right)\big|_{S_{op}}$ at the interface, such that

$$\sum_{j=1}^{N} a_j \phi_j(\vec{x}) = \sum_{m=1}^{M} b_m \varphi_m(\vec{x}). \tag{14}$$

Multiplying $\psi_\mu(x)$ on both sides of Eq. (14) and integrating over the cavity opening S_{op} results in:

$$\sum_{i=1}^{N} a_i \delta_{i_x,\mu} \psi_{i_y}(0) = \sum_{m=1}^{M} b_m \left[\int_0^{L_x} \psi_\mu(x) \varphi_m(\vec{x}) dS_{op} \right]. \tag{15}$$

where $\delta_{i,j}$ is the Kronecker delta function and i_x is the i-th acoustic modal index in the x direction.

By defining $Z_{\mu,m} = \int_0^{L_x} \psi_\mu(x) \varphi_m(\vec{x}) dS_{op}$ as the radiation impedance of the opening [26], Eq. (15) can be rewritten as:

$$\sum_{i=1}^{N} a_i \delta_{\mu,i_x} \psi_{i_y}(0) = \sum_{m=1}^{M} b_m Z_{\mu,m} . \tag{16}$$

To solve for the coefficients a_i and b_m, the second Green identity is applied to the cavity space Ω_a, as follows

$$\int_{\Omega_a} p_a \nabla^2 \phi_i d\Omega_a - \int_{\Omega_a} \phi_i \nabla^2 p_a d\Omega_a + \int_S \phi_i \frac{\partial p_a}{\partial n} ds - \int_S p_a \frac{\partial \phi_i}{\partial n} ds = 0 , \tag{17}$$

where the volume integral covers the entire domain Ω_a, and the surface integral is evaluated on the entire boundary surface of Ω_a, including the cavity and the resonator openings.

Substituting Eqs. (1) - (5), and (11) into Eq. (17), we obtain

$$\begin{aligned} &\sum_{j=1}^{N} \left[a_j \left(k^2 - k_i^2\right) \int_V \left(\phi_i \phi_j\right) dv \right] - i\rho k c_0 \int_{S_{op}} \left(\phi_i v_n\right) ds_{op} \\ &= -i\rho k c_0 q_s \phi_i(\vec{x}_s) + \sum_{t=1}^{T} \frac{i\rho k c_0}{Z_t} \int_{S_R} \left[\phi_i \sum_{h=1}^{N} a_h \phi_h \delta\left(\vec{x} - \vec{x}_t^R\right) \right] ds_R \end{aligned} . \tag{18}$$

Eq. (18) considers the interactions between the open cavity and multiple resonators, in which the cavity opening effect on the cavity-resonator system acoustic coupling is indicated by the normal particle velocity v_n.

Using the orthogonal properties, Eq. (18) can be simplified to

$$\begin{aligned} & a_i\left(k^2-k_i^2\right)-i\rho k c_0 \sum\nolimits_{m=1}^{M} b_m \delta_{i_x,m} \psi_{i_y}\left(0\right) \\ & = -i\rho k c_0 q_s \phi_i\left(\vec{x}_s\right)+\sum\nolimits_{t=1}^{T} \frac{i\rho k c_0}{Z_t^R} \int_{S_R}\left[\phi_i \sum\nolimits_{h=1}^{N} a_h \phi_h \delta\left(\vec{x}-\vec{x}_t^R\right)\right] ds_R \end{aligned}, \tag{19}$$

By setting $\mathbf{A}=\left\{a_1,a_2,\cdots,a_N\right\}^T$ and $\mathbf{B}=\left\{b_1,b_2,\cdots,b_M\right\}^T$, the Eq.(16) and Eq.(19) can be rearranged as follows:

$$\mathbf{\Phi A}=\mathbf{ZB}, \tag{20}$$

$$\left(\mathbf{K}-\mathbf{Z^R}\right)\mathbf{A}-\mathbf{MB}=\mathbf{S}, \tag{21}$$

where

$$\mathbf{S}=-i\rho k c_0 q_s \begin{Bmatrix} \phi_1\left(\vec{x}_s\right) \\ \phi_2\left(\vec{x}_s\right) \\ \vdots \\ \phi_N\left(\vec{x}_s\right) \end{Bmatrix}, \tag{22}$$

$$\mathbf{K}=\begin{bmatrix} k^2-k_1^2,0,0,\cdots,0 \\ 0,k^2-k_2^2,0,\cdots,0 \\ \ddots \\ 0,0,\cdots,k^2-k_N^2 \end{bmatrix}, \tag{23}$$

$$\mathbf{M}=i\rho k c_0 \begin{bmatrix} \delta_{1_x,1}\psi_{1_y}\left(0\right),\delta_{1_x,2}\psi_{1_y}\left(0\right),\cdots,\delta_{1_x,M}\psi_{1_y}\left(0\right) \\ \delta_{2_x,1}\psi_{2_y}\left(0\right),\delta_{2_x,2}\psi_{2_y}\left(0\right),\cdots,\delta_{2_x,M}\psi_{2_y}\left(0\right) \\ \ddots \\ \delta_{N_x,1}\psi_{N_y}\left(0\right),\delta_{N_x,2}\psi_{N_y}\left(0\right),\cdots,\delta_{N_x,M}\psi_{N_y}\left(0\right) \end{bmatrix}, \tag{24}$$

$$
\mathbf{Z}^{\mathbf{R}} = i\rho k c_0 \begin{bmatrix} \frac{1}{Z_1}, 0, \cdots, 0 \\ 0, \frac{1}{Z_2}, \cdots, 0 \\ \ddots \\ 0, 0, \cdots, \frac{1}{Z_T} \end{bmatrix} \begin{bmatrix} \phi_1\left(\vec{x}_1^R\right), \phi_1\left(\vec{x}_2^R\right), \cdots, \phi_1\left(\vec{x}_T^R\right) \\ \phi_2\left(\vec{x}_1^R\right), \phi_2\left(\vec{x}_2^R\right), \cdots, \phi_2\left(\vec{x}_T^R\right) \\ \ddots \\ \phi_N\left(\vec{x}_1^R\right), \phi_N\left(\vec{x}_2^R\right), \cdots, \phi_N\left(\vec{x}_T^R\right) \end{bmatrix} \begin{bmatrix} \phi_1\left(\vec{x}_1^R\right), \phi_2\left(\vec{x}_1^R\right), \cdots, \phi_N\left(\vec{x}_1^R\right) \\ \phi_1\left(\vec{x}_2^R\right), \phi_2\left(\vec{x}_2^R\right), \cdots, \phi_N\left(\vec{x}_2^R\right) \\ \ddots \\ \phi_1\left(\vec{x}_T^R\right), \phi_2\left(\vec{x}_T^R\right), \cdots, \phi_N\left(\vec{x}_T^R\right) \end{bmatrix}, \qquad (25)
$$

$$
\mathbf{\Phi} = \begin{bmatrix} \delta_{1_x,1}\psi_{1_y}(0), \delta_{2_x,1}\psi_{2_y}(0), \cdots, \delta_{N_x,1}\psi_{N_y}(0) \\ \delta_{1_x,2}\psi_{1_y}(0), \delta_{2_x,2}\psi_{2_y}(0), \cdots, \delta_{N_x,2}\psi_{N_y}(0) \\ \ddots \\ \delta_{1_x,M}\psi_{1_y}(0), \delta_{2_x,M}\psi_{2_y}(0), \cdots, \delta_{N_x,M}\psi_{N_y}(0) \end{bmatrix}, \qquad (26)
$$

$$
\mathbf{Z} = \begin{bmatrix} \int_0^{L_x} \psi_1(x)\varphi_1(x,0)\,dx, \int_0^{L_x} \psi_1(x)\varphi_2(x,0)\,dx, \ \dots\ , \int_0^{L_x} \psi_1(x)\varphi_M(x,0)\,dx \\ \int_0^{L_x} \psi_2(x)\varphi_1(x,0)\,dx, \int_0^{L_x} \psi_2(x)\varphi_2(x,0)\,dx, \ \dots\ , \int_0^{L_x} \psi_2(x)\varphi_M(x,0)\,dx \\ \ddots \\ \int_0^{L_x} \psi_{N_x}(x)\varphi_1(x,0)\,dx, \int_0^{L_x} \psi_{N_x}(x)\varphi_2(x,0)\,dx, \ \dots\ , \int_0^{L_x} \psi_{N_x}(x)\varphi_M(x,0)\,dx \end{bmatrix}. \qquad (27)
$$

The coefficient matrices $\mathbf{A}$ and $\mathbf{B}$ can be obtained after solving the above equations so that the sound pressure p_a and p_b can be determined.

3. Performance of tunable parallel barriers using HR

3.1 Model validation

In this section, a numerical simulation is investigated in order to examine the accuracy of the theoretical model. The parallel barriers considered in this paper have a size of L_x =1.83 m and L_y =1 m, which are similar to the configurations studied in Refs. [2, 11]. The barrier wall thickness is 0.1 m. In order to verify whether the contribution of the acoustic modes can represent the sound pressure field at all frequencies, the SPL spectrum at the receiving point R1=(5, -0.9) m for the parallel barriers without the HR is compared to the prediction using the BEM. Modal truncation is required in the actual calculation. In Eq. (4), 400 enclosed-cavity modes are used to calculate the sound field in the rectangular cavity Ω_a. For the vibration mode in Eq.(11), the subscript m ranges from 0 to 30. The numerical results indicate that the number of modes is normally sufficient, as a further increase in the number does not make a significant difference for this study.

It is challenging to obtain the external mode function $\varphi_m(\vec{x})$ analytically owing to the difficulty in determining the Green's function. In this regard, numerical software package COMSOL Multiphysics which is based on finite element method is used to get $\varphi_m(\vec{x})$. In the numerical simulation, the infinite space Ω_b is firstly truncated by the perfectly matched layer (PML) to a confined one. The PML enables the outgoing wave to leave the domain with a minimal spurious reflection at the artificial boundaries. The m-th vibration mode of $\psi_m(x)$ is set at the cavity opening and 500 nodes are used to discretize the $S_{\mathrm{op.}}$ The acoustic domain Ω_b is discretized using triangular elements and mesh size is chosen to be less than one twelfth of an acoustic wavelength of the upper limit frequency here (1000Hz). The calculated frequency range in the current study is from 30 to 1000 Hz with a step size of 1 Hz. Subsequently, the values of $\varphi_m(\vec{x})$ can be acquired and substituted into Eq.(27) so that matrix of **Z** can be found for solving coefficient matrices **A** and **B**.

Fig. 3 presents the comparison of the sound pressure spectrum between the proposed theoretical model and BEM. In general, quite a good agreement is observed. The dashed line indicates the results predicted by the trapped modes as used in Ref. [2], and it can be found that the use of trapped modes achieves agreement with the BEM only at the resonant peaks, while significant discrepancies appear in the non-resonant region. This indicates that additional trapped modes with higher radiation loss should be considered when using the trapped modes to reproduce the sound field. However, PML-constructed eigenvalues solution generates a multitude of spurious eigenvalues that are very difficult to distinguish [27]. As a result, it is challenging to construct the sound field inside or outside the parallel barriers by using the trapped modes. As illustrated in Fig. 3, the results obtained by the proposed theoretical model agree well with the BEM results; therefore, it is used in the subsequent studies.

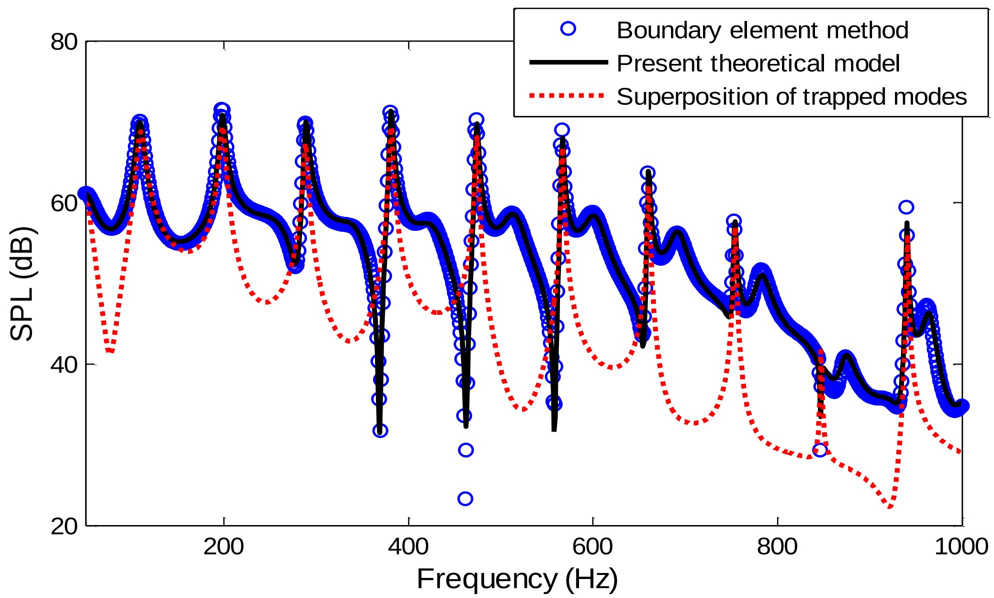

Fig. 3. Comparison among the present theoretical model, boundary element method (BEM) and method of superposition of trapped modes for prediction of sound pressure level.

3.2 Performance of HR mounted on parallel barriers

When the HR is mounted on the barrier walls, the sound pressure spectrum and acoustic modal response in the two spaces Ω_a and Ω_b are changed significantly. In this paper, the HR model is named HR with a number representing the natural frequency of the resonator. In order to reduce the SPL at one peak at 289 Hz, a HR281 is designed and located at (0, -0.9) m. The resonator used is the typical T-shaped acoustic resonator, which consists of a short neck branch and long body branch, as illustrated in Fig.1. The physical length of the neck branch is L_{b1} = 10 mm, while that of the body branch is L_{b2} = 55 mm. The neck and body branch diameters are d_1= 20 mm and d_2= 50 mm, respectively. The output impedance at the aperture of such a resonator can be calculated based on the method proposed by Ref. [13].

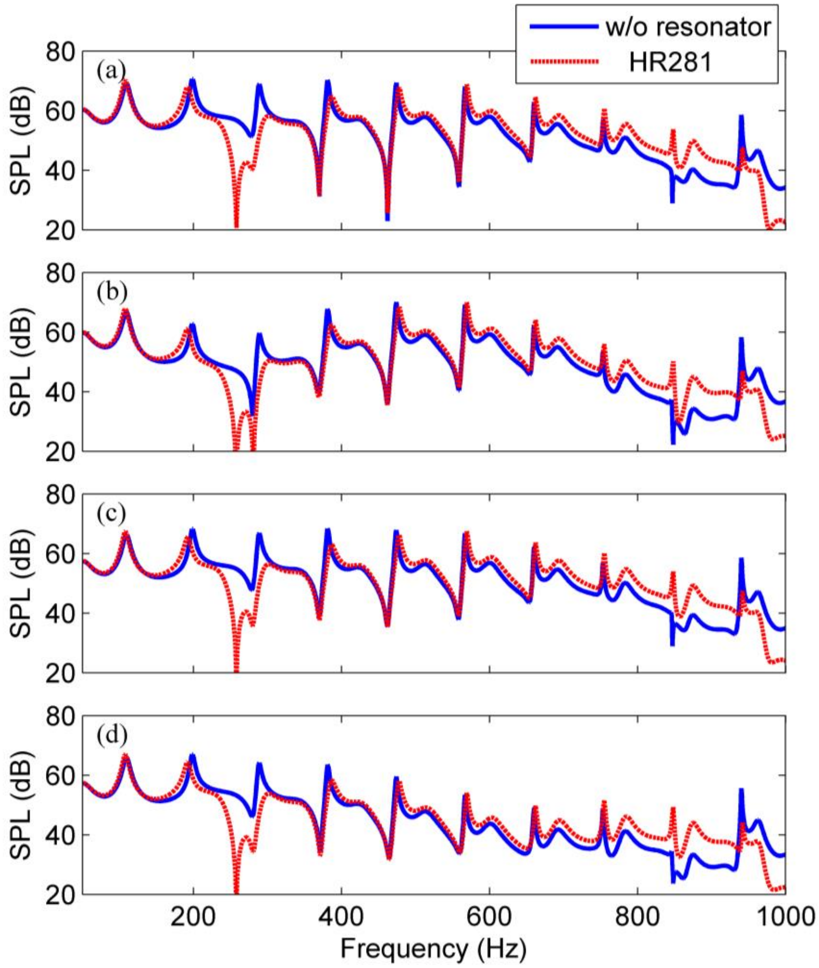

Fig. 4. Comparison of SPLs at different receiving points for the parallel barriers with and without HR281. (a) receiver at (5, -0.9) m; (b) receiver at (5, 0) m; (c) receiver at (10, -0.9) m and (d) receiver at (10, 0) m.

Fig. 4 depicts the SPLs for the parallel barriers with and without HR281 at the receiving point R1 = (5, -0.9) m, R2 = (5, 0) m, R3 = (10, -0.9) m, and R4 = (10, 0) m. Multiple peaks are observed for the parallel barriers with rigid walls at each receiver. The SPLs around the target peak of 289 Hz are significantly suppressed using HR281. As illustrated in Fig. 4(a), the SPL is reduced from 68.93 dB to 51.79 dB at 289 Hz, and a noise reduction of 17.14 dB occurs. This is attributed to the change in the responses of the acoustic cavity mode (3, 0) and external mode (4), which are dominated at 289 Hz. A strong acoustic coupling occurs between the HR and open cavity, and noise reduction can therefore be achieved. Furthermore, noise reduction is observed within the frequency range of approximately 198 Hz and 381 Hz. However, when integration with HR281 is applied, the performance appears to deteriorate at a frequency range mainly around 847 Hz. As indicated in Fig 3 (a), the SPL at 847 Hz is increased from 28.95 dB to 51.38 dB after inserting the HR281. The mechanism of the sound spectrum changes that occur following insertion of the resonator is presented in the next section. In order to perform the analysis, the R1 at (5, -0.9) m is selected as the typical receiver. The SPL variation at R1 is used to represent the sound field changes following the resonator insertion.

3.3 SPL peak and acoustic modal analysis

In order to understand the noise suppression mechanism behind the barrier when inserting the HR into the parallel barriers, the SPL distribution of the peaks and acoustic modal response are discussed in this section. A total of 30 modes are used in Eq.(12) for predicting the SPL behind the barrier.

Table 1
The comparison of the eigenvalues of the first ten (m, 0) enclosed cavity modes and the frequencies of the sound pressure level for a parallel barriers.

Enclosed-cavity		Trapped modes of open cavity	Parallel Barriers	
Modal indices	Frequency	Frequency	Peaks	Frequency
(i_x,i_y)	Hz	Hz		Hz
(1,0)	93.72	109.51+4.27i	2	109
(2,0)	187.43	198.42+2.87i	3	198
(3,0)	281.15	288.44+2.3i	4	289
(4,0)	374.86	381.23+1.74i	5	381
(5,0)	468.58	473.95+1.44i	6	474
(6,0)	562.3	566.96+1.11i	7	567
(7,0)	656.01	660.24+1.06i	8	660
(8,0)	749.73	753.68+0.95i	9	753
(9,0)	843.44	847.2+0.79i	-	-
(10,0)	937.16	940.69+0.64i	10	940

Fig. 5(a) to Fig 5(i) illustrate the SPL distributions at 109 Hz, 198 Hz, 289 Hz, 381 Hz, 474 Hz, 567 Hz, 660 Hz, 753 Hz, and 940 Hz, respectively, when the source is located at (0.1, -0.9) m. It can be observed that the sound distributions within the bounded domain at these frequencies are similar to their corresponding modal shapes of the enclosed cavity. In addition to this, the peak frequency is close to the resonance frequency of the enclosed cavity.

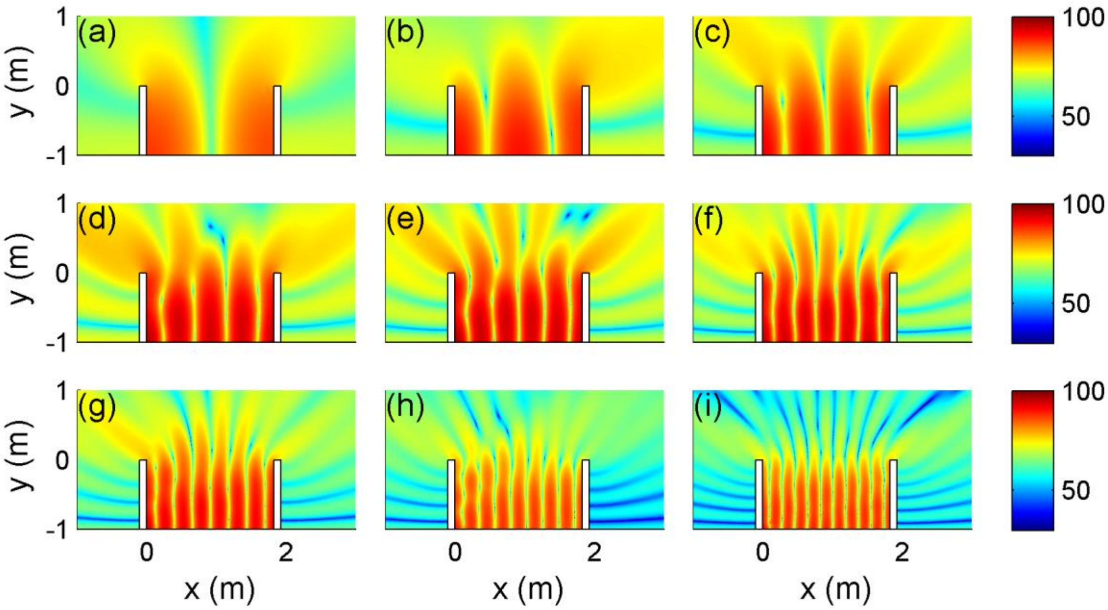

Fig. 5. The SPL distributions between parallel barriers with the sound source at (0.1, -0.9) m for the frequency (a) f=109 Hz; (b) f =198 Hz; (c) f =289 Hz; (d) f =381 Hz; (e) f =474 Hz; (f) f =567 Hz; (g) f =660 Hz; (h) f =753 Hz and (i) f =940 Hz.

Fig. 6 illustrates the modal coefficients $\left|a_j\right|$ and $\left|b_m\right|$ of the parallel barriers with and without the resonator HR281 at the location of (0, -0.9) m. Fig. 6(1a) and Fig. 6(1b) respectively display the modal coefficients $\left|a_j\right|$ and $\left|b_m\right|$ at 289 Hz which corresponding to the peak in SPL spectrum. Fig. 6(2a) and Fig. 6(2b) indicate the modal coefficients $\left|a_j\right|$ and $\left|b_m\right|$ at 847Hz which is the trough point in SPL spectrum. It can be observed that, at 289 Hz, the sound field inside the cavity space Ω_a without a HR is dominated by the cavity mode (3, 0), while the sound response in the semi-infinite space Ω_b is dominated by the external mode (4). For 847 Hz, the dominant cavity mode inside the parallel barriers is (9, 0) while responses of the sixth to tenth external mode contribute mainly to the sound field in Ω_b. In order to control the SPL peak at 289 Hz, a HR281 is designed for suppressing the response of the enclosure mode (3, 0) and mounted on the barrier. After inserting the HR281, the modal responses $\left|a_{3,0}\right|$ and $\left|b_4\right|$ at 289 Hz are significantly suppressed. A relationship exists between the number of external modal indexes and modal number of the enclosed cavity at the peak frequency. In order to reduce the noise level which is dominant by the *m*-th external mode, the response for the enclosed cavity mode (*m*-1, 0) needs to be suppressed. For the frequency of 847 Hz, the modal amplitude of cavity mode (9, 0) and tenth external mode are significantly enhanced.

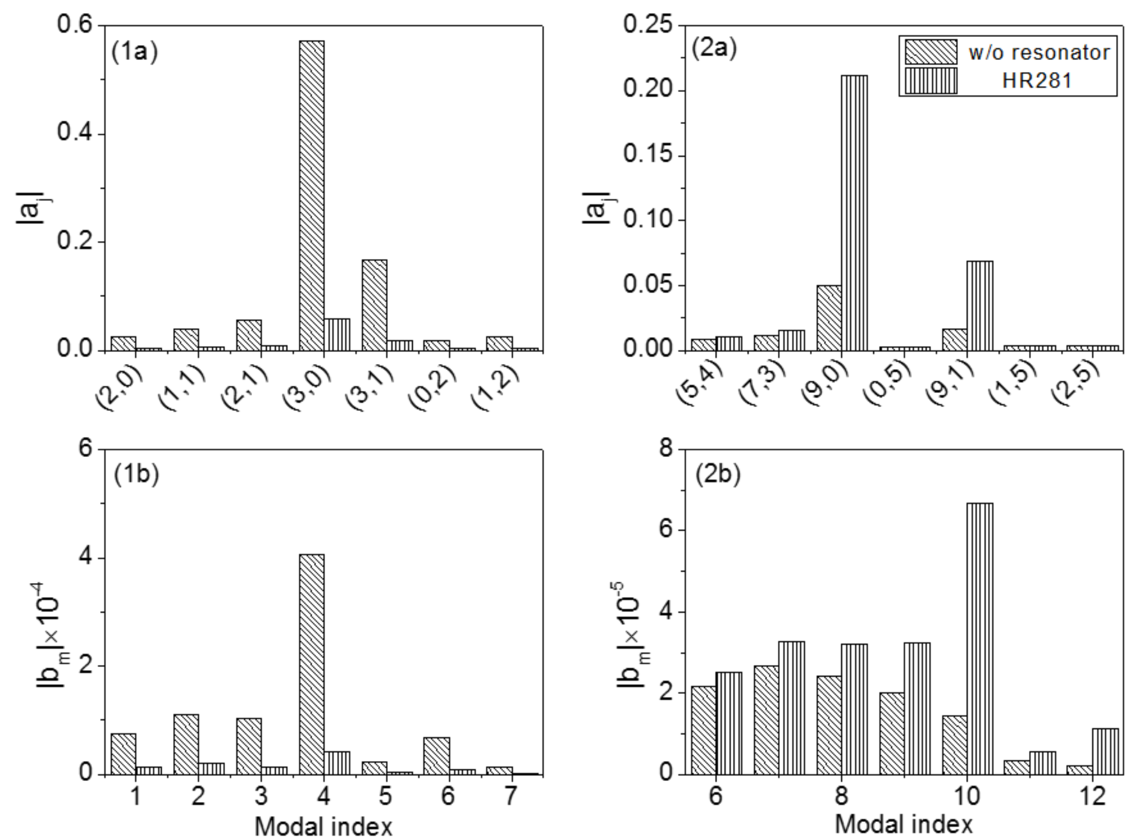

Fig. 6. Comparison of amplitudes of the enclosed cavity mode and external mode for the parallel barriers with and without HR281. (1a) $|a_j|$ for 289 Hz (1b) $|b_m|$ for 289Hz, (2a) $|a_j|$ for 847Hz and (2b) $|b_m|$ for 847 Hz.

Fig. 7(1a) and Fig. 7(2a) provide a comparison of the sound pressure level distributions for 289 Hz before and after the installation of a HR281, respectively. The sound field pattern appears similar, while the amplitude different. In general, the SPL is reduced significantly inside and outside the parallel barriers. Fig. 7(1a) indicates that the SPL in the shadow zone of the parallel barriers without a resonator is more than 65 dB, while Fig. 7(2a) indicates that the SPL for the barrier with a HR281 is roughly less than 55 dB. A noise reduction of approximately 10 dB occurs, which manifests the advantage of using HR to improve the noise reduction in the shadow zone. Fig. 7(1b) illustrates that, at 847 Hz, the dominant nodal line is located near the sound source position, so the SPL between or behind the parallel barriers is relatively low. When HR281 is inserted, the resonator behaves like a secondary sound source, and the radiated wave from the HR aperture influences the sound field between the barriers. Consequently, the acoustic mode pattern inside the cavity domain Ω_a is distorted and the nodal line is shifted away from the sound source position, as shown in Fig. 7(2b). Therefore, the performance of the parallel barriers integrated with the HR deteriorates. The sound pressure level at 847 Hz increases from 28.95 dB to 51.38 dB after inserting the HR281 at receiver R1.

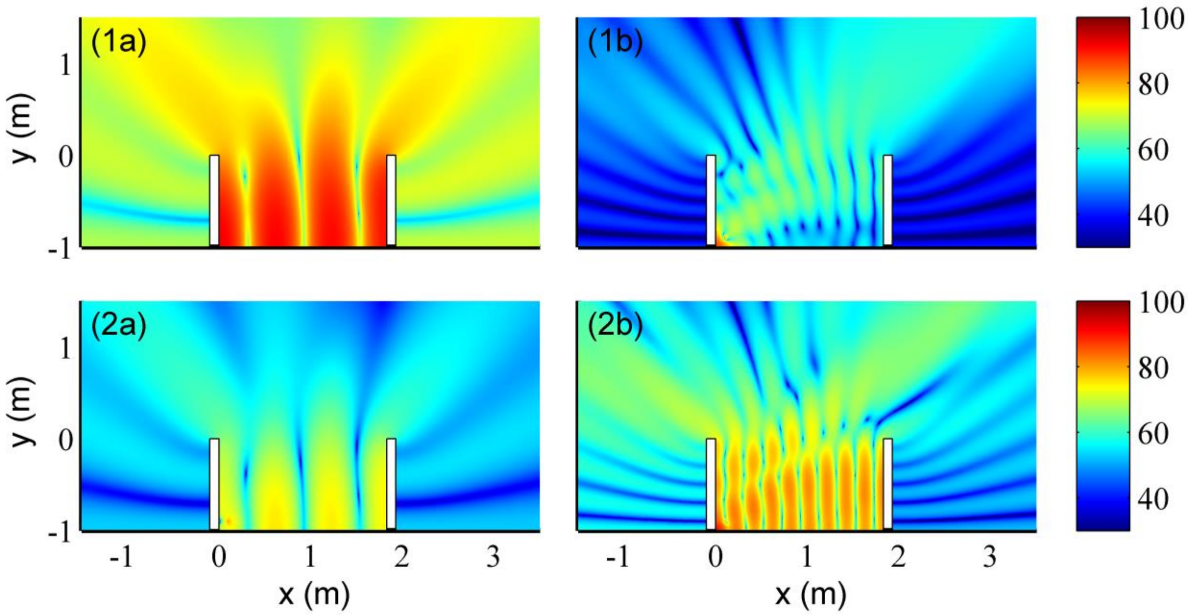

Fig. 7. The sound pressure level distributions for the parallel barriers with and without HR281: (1a) and (1b) without the resonator for f=289Hz and f=847Hz respectively; (2a) and (2b) with

HR281 for *f*=289Hz and *f*=847Hz respectively.

3.4 Variation with different HR locations.

The interaction between the resonator and bounded domain Ω_a has an impact on the sound radiation from the cavity opening S_{op}. In order to achieve optimal noise abatement performance, the effect of a given resonator location is investigated in this section. Important factors can be observed in Eq. (19), which can be further simplified after neglecting the non-target modes as follows:

$$a_i \frac{\left(k^2-k_i^2\right)}{i\rho kc}+\frac{Z^R\left(q_s\phi_i\left(\vec{x}_s\right)-\sum_{m=1}^{M} b_m Z_{im}\right)}{Z^R-i\rho kc\frac{\left[\phi_i\left(\vec{x}^R\right)\right]^2}{\left(k^2-k_i^2\right)}}=0\,. \quad (28)$$

The value of Z^R and $\phi_i\left(\vec{x}^R\right)$ in Eq. (25) influences the acoustic modal responses a_i and b_m, indicating that the noise reduction is sensitive to the location and output impedance of the resonator. For a given geometry of resonator, its output impedance is fixed but its location can be varied. Traditionally, the resonator is set at the anti-nodal surfaces, where a very strong acoustic coupling occurs between the resonator and cavity, and as such, the SPL at the target frequency can be suppressed effectively; however, the SPL in the vicinity of the target frequency may be increased. With the aim of achieving sound reduction within a selected frequency band, the optimal resonator location was determined. Owing to the space limitation, the resonator should be mounted on the barrier walls.

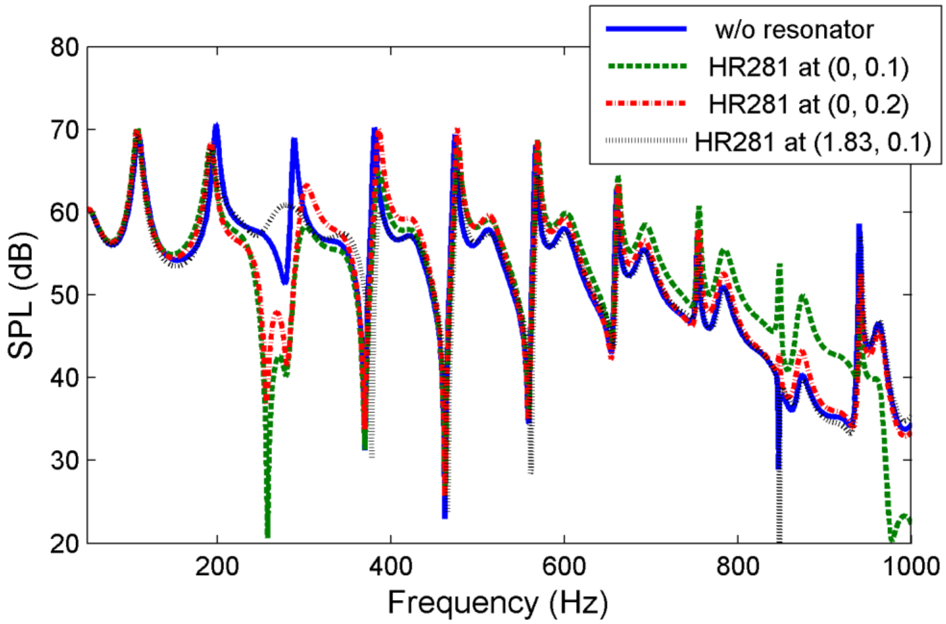

Fig. 8. Variation of SPL spectrum when HR281 at different positions.

Fig. 8 illustrates the variation of the SPL spectrum when the HR281 mounted at different location. The solid line indicates the SPL at the receiver R1 without the resonator. The dashed, dot-dashed and dotted lines represent the SPL changes when the mouth center of a single HR281 is mounted at (0, -0.9) m, (0, -0.8) m, and (1.83, -0.9) m, respectively. When the resonator is located at (0, -0.9) m, which is close to the sound source (x_s=0.1 m, y_s=-0.9 m), the sound peak at 289 Hz is suppressed by 17.14 dB and the frequency range for noise reduction over 10 dB is 248 Hz to 292 Hz. However, the SPL in the high frequency range is notably increased. When the resonator is moved upward to (0, -0.8) m, noise reduction can also be observed in the frequency range of 196 Hz to 297 Hz, and a slight increment of the SPL occurs at the frequency range around 847 Hz. When the HR281 is installed at (1.83, -0.9) m, which is on the right-hand side of the parallel barriers, although a certain reduction can be observed at the peak of 289 Hz, the change at the other frequency is not obvious. The above results indicate that when the resonator is located closer to the primary sound source, the acoustic coupling between the sound source and resonator will be stronger; hence, the noise reduction at the target frequency and within its vicinity will be higher. Among these three locations, (0, -0.8) m is the superior option in terms of the noise reduction in amplitude and bandwidth. The above analysis also demonstrates that, with appropriate resonator positioning, the SPL at the target frequency can be reduced, while that in the higher frequency range will not be increased. In this regard, it is necessary to optimize the HR location such that the noise reduction is high and the frequency band is also wide. The performance of the parallel barriers can be characterized by the highest mean insertion loss (IL_{mean}) within a target frequency range. Mathematically, it is expressed as follows:

$$\max\left(IL_{mean}\left(f\right)\right) \text{ and } IL_{mean} = \frac{\sum_{f_L}^{f_U}\left(SPL_{Rigid}\left(f\right)-SPL_{HR}\left(f\right)\right)}{N_f}, \qquad (29)$$
$$subject\ to: f_L \le f \le f_U$$

where SPL is the sound pressure level, and the subscripts ‘Rigid’ and ‘HR’ represent the parallel barriers without and with the HR respectively. N_f is the total number of sampling frequencies used to calculate the SPL. The $\left[f_L, f_U\right]$ is set to be [279, 299] Hz for low frequency band and [837, 857] Hz for the high frequency band respectively.

Fig. 9 indicates the variation of IL_{mean} at receiving point R1 when the HR281 is placed at different mounting heights of the barrier wall. The results for the low frequency band [279,299] Hz and for the high frequency band [837, 857] Hz is represented by a solid line and dashed line, respectively. Fig. 9(a) and Fig. 9(b) illustrate the results for the HR281 mounted on the left-hand and right-hand sides of the parallel barriers, respectively. As shown in Fig. 9(a), IL_{mean} in the frequency range of [279, 299] Hz increases when it is mounted from 0.01 m to 0.12 m, and then it drops to approximately 0 dB when the HR281 is mounted at 0.62 m above ground. In order to achieve noise reduction in the frequency range of [279, 299] Hz, the HR281 should be mounted at a height lower than 0.62 m from the ground. The maximum of IL_{mean} is found to be about

10.48 dB when the HR281 is located 0.12 m above ground. However, IL_{mean} in the frequency range of [837, 857] Hz increases from a negative value to near zero when the HR is mounted from 0.01 m to 0.43 m from the ground. When the HR281 is mounted at 0.12 m from the ground, IL_{mean} is about -2.94 dB in the frequency range of [837, 857]. In order to obtain a maximum IL_{mean} in both [279,299] Hz and [837, 857] Hz, the optimal location for the single HR281 should be 0.1 to 0.2 m above ground on the left-hand side of the parallel barriers. When HR281 is mounted on the right-hand side of the parallel barriers, noise reduction can be identified in [279,299] Hz at any height. The maximum IL_{mean} = 5.91 dB is found when the resonator is at (1.83, -0.7) m and there is a slight change in IL_{mean} at [837, 857] Hz for different locations of HR281.

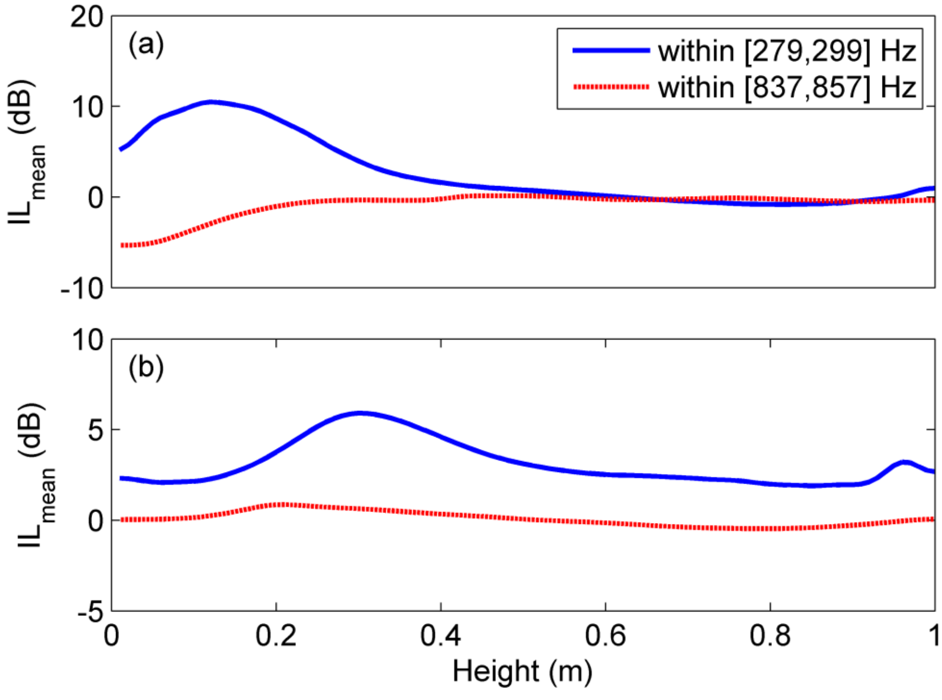

Fig. 9. Optimization curve of IL_{mean} for different mounting locations of the HR281. (a) HR281 is mounted on the left-hand side of parallel barriers and (b) HR281 is mounted on the right-hand side of parallel barriers.

3.5 Diffraction point

The purpose of this study is to reduce the sound pressure level at the receiving point behind the barriers. In addition to investigating the change in the acoustic modal response in the above-section, the diffraction efficiency around the open region is studied using diffraction theory, which is suggested by Keller [28]. The influence on the sound diffraction when using a HR integrated into a parallel barrier is very important, because only diffracted waves propagate into the shadow zone. The diffraction field is determined by the acoustical property of the sound field at the diffracting point and the diffraction coefficient D [28].

$$p_d = Dp_i r^{-1/2} e^{ikr}, \tag{30}$$

where p_d and p_i are the sound pressure at the receiving and diffracting points, and r is the distance from the diffraction point to the receiving point. When incident waves from the sound source inside the bounded domain Ω_a impinge on the barrier top, the sound field at the barrier top edge will become a secondary source that generates diffracting waves. In this regard, the sound pressure at the receiving point in the shadow zone is related to that at the diffraction point. As the thickness of the barrier used is 0.1 m, which is significantly smaller than the wavelength of the frequency of interest, the top edge of the barrier is simply assumed to be a diffraction point. The diffraction coefficient D is related to the directions of the incident and diffracting rays, wavelength, and geometrical and media physical properties at the diffraction point. An asymptotical expanded form of the diffraction coefficient D is

$$D = -\frac{e^{i\pi/4}}{2(2\pi k)^{1/2}}\left[\sec\left(\frac{\alpha-\theta}{2}\right)+\sec\left(\frac{\alpha+\theta}{2}\right)\right], \tag{31}$$

where α and θ are the angles of incidence and diffraction, respectively. As indicated in Eq. (31), the diffraction coefficient is low for high frequencies. As a result, the sound pressure at the receiver has a descending trend with the increasing of frequency. Moreover, with a fixed frequency, the diffraction coefficient increases when the incident angle α is increased. This means that the sound wave is diffracted more effectively if the incident wave impinges normally to the barrier surface, and as a result, the maximum diffraction coefficient is obtained. If the incident wave impinges in a parallel direction (at a grazing angle) with the barrier surface, a minimum diffraction coefficient will be observed.

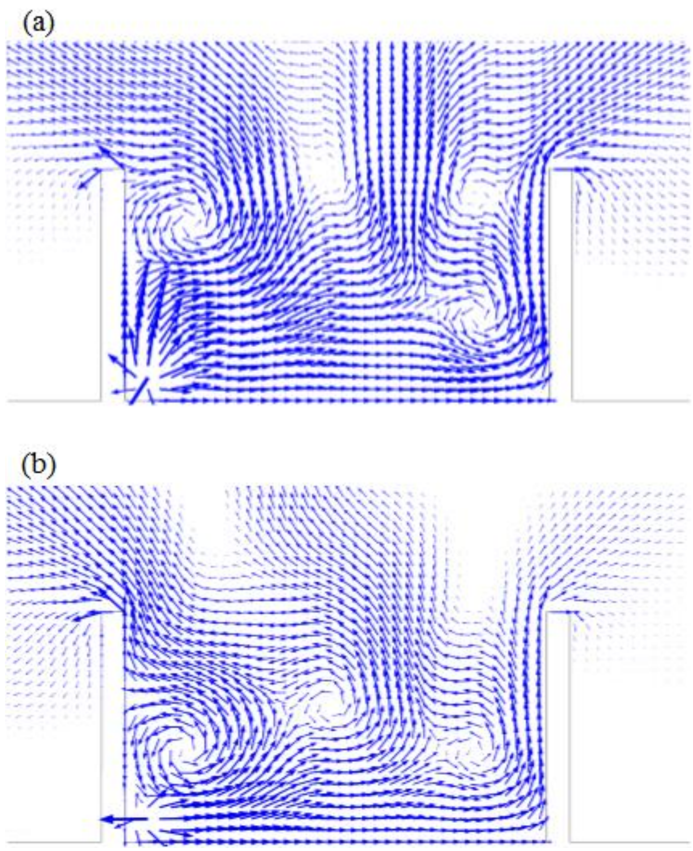

Fig. 10. Comparison of sound intensity distributions of the parallel barriers with and without HR281 at 289 Hz: (a) without the resonator and (b) with the HR281 at (0, -0.9) m.

In order to investigate the variation of the diffraction field at the barrier top edge with the use of a HR, the sound intensity field at the peak frequency of 289 Hz is displayed in Fig. 10. It should be noted that the scale factor of the sound intensity field in Fig. 10(a) is 100:1, while that in Fig. 10(b) is 1000:1. In other words, with the same arrow length, the actual amplitude in

Fig.10(a) is 10 times that in Fig. 10(b). The arrow length around the edge top of the right-hand side of the parallel barriers in Fig. 10(b) is shorter than that in Fig. 10 (a), which indicates that the sound intensity in this region is reduced by approximately 1/10 when a single HR281 is installed. Comparing the direction of the incident and diffracted waves around the barrier top edge, the incidence angle at the top edge of the wall is slightly bent parallel to the vertical wall when a HR281 is installed. Therefore, the diffraction coefficient D is slightly reduced. Because both p_i and D are reduced at the top edge of the barrier, noise reduction can be achieved in the shadow zone on the right-hand side of the parallel walls, and a similar change can be observed on the left-hand side of the parallel barriers. Therefore, by mounting a HR at a location close to the sound source, the sound reduction can be achieved in the shadow zones of both sides of the parallel barriers.

3.6 Design of several HRs

An array of resonators can be used to reduce the noise level at multiple resonant frequencies. According to previous studies on optimization of a single HR281, the optimal location is at (0, -0.8) m. In this section, two resonators with different natural frequencies were installed on the barrier walls. The models of HR281 and HR468, targeted for sound peaks at 289 Hz and 474 Hz, respectively were adopted. The performances of these two Helmholtz resonators at two different positions were studied: case (1) HR281 at (0, -0.8) m and HR 468 at (1.83, -0.95) m, and case (2) HR281 at (1.83, -0.8) m and HR468 at (1.83, -0.95) m. Fig. 11 illustrates the variation in the SPL spectrum at the receiving point (5, -0.9) m after these two combinations of HRs. Multiple peaks are found to be suppressed in the frequency range beyond 200 Hz in both cases. For case (1), the corresponding peaks at 289 Hz and 474 Hz are reduced by 12.39 dB and 19.84 dB respectively. For case (2), noise reductions of 13.36 dB and 24.53 dB can be observed at their peak frequencies. Moreover, the SPL at other peaks, which are off-target frequencies, are notably reduced. This is owing to the fact that the modal responses at these peaks were modified after integration with these two resonators. In general, with the use of two different resonators at various locations, the SPL at the receiving point is reduced and the stopband can be widened effectively. Comparing different locations of HRs, the case (1) of HR281 at (0, -0.8) m and HR468 at (1.83, -0.95) m exhibits superior noise reduction performance.

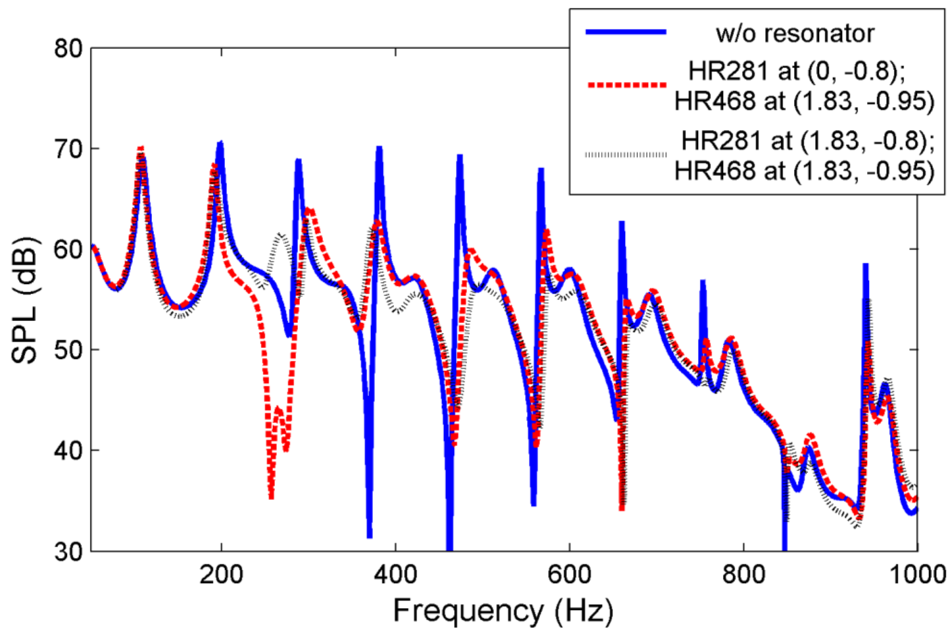

Fig. 11. Comparison of SPL for parallel barriers with and without two Helmholtz resonator models at different positions.

4. Experimental validation

In order to examine the feasibility of the usage of Helmholtz resonators integrated into the parallel barriers, a series of experiments was conducted. The experiments were carried out in an anechoic chamber with an effective size of 6 m (length) ×6 m (width) ×4 m (height). The experimental set-up for the parallel barriers in the one-fifth scaled down model is shown in Fig.12. The parallel barriers and ground surfaces were made of 18.5mm thick wooden boards with varnishing. The barriers were 1 m in height and 4.8 m in length and were placed parallel to each other at a distance of 1.83 m. Prior measurements have demonstrated that these wooden boards can be treated as a perfectly reflecting surface [29]. A Tannoy speaker mounted on a long brass pipe with a length of l.5 m and diameter of 25 mm was used to simulate a point sound source as shown in Fig. 12(b). Measurement of the directional characteristic of this point source was conducted and it was found that the deviation in all directions was within 1 dB for all frequencies above 200 Hz. The point sound source was located 0.1 m away from one of the barriers and at a height of 0.1 m above ground. One B&K 4189 microphone, connected to a NI 9234 preamplifier and a B&K NEXUS conditional amplifier, was employed to capture the acoustic signal. The location of the microphone was chosen at 1 m behind the barrier and at a height of 0.2 m above ground. The experimental set-up of the parallel barriers was a three-dimensional configuration and therefore it was difficult to change the sound field between the parallel barriers practically by using a single resonator. In this case, five HR281 resonators were evenly distributed along the parallel barriers. The resonators were made of aluminum which is regarded as acoustically rigid. The sound pressure level was then measured behind the parallel barriers with and without these resonators.

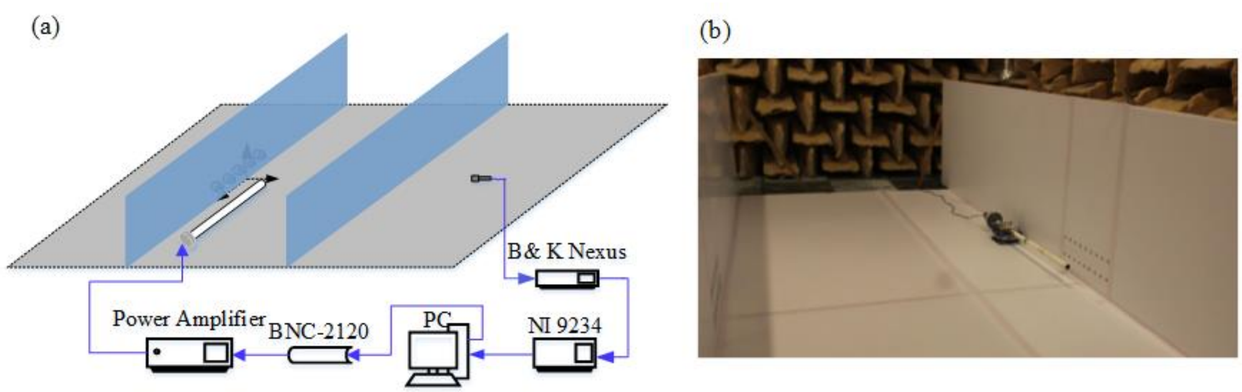

Fig. 12. Sound response measurement system. (a) Experimental set-up and (b) photo.

Fig. 13 shows the measured sound pressure level spectrum for a parallel barriers with and without installation of resonators. It is noted the original sound peak appears at 291 Hz. This can be explained by the fact that the opening in the *z*-direction increases the radiation loss and results in a higher coupling frequency. The sound pressure level at this peak was reduced from 78.66 dB to 75.49 dB and noise reduction of over 3 dB could be obtained. Apart from the reduction at the sound peak, the sound pressure level in the frequency range of 251 Hz to 295 Hz decreased by about 4.36 dB on average. Although the sound pressure level spectrum is different from the prediction model in the two-dimensional configuration, the experimental results proved that the use of Helmholtz resonator integrated into the parallel barriers can improve the noise reduction in the shadow zone at the target degradation frequency.

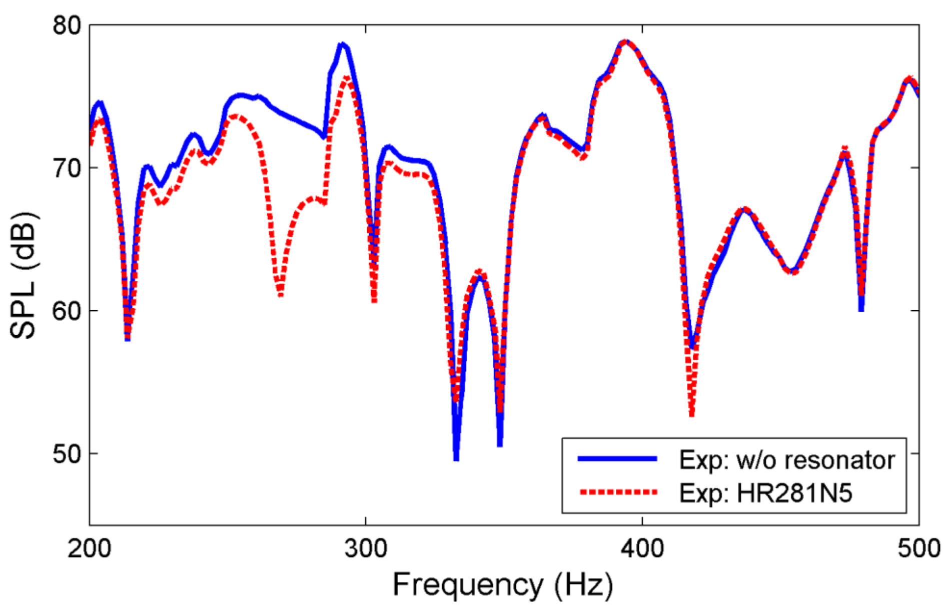

Fig. 13. Experimental results of SPL for the parallel barriers with and without HR281.

5. Conclusions

The performance of a parallel barrier integrated with a Helmholtz resonator has been investigated theoretically and experimentally. The benefits offered by the Helmholtz resonator to the parallel barriers include the suppression of the sound pressure level at specific frequencies corresponding to the resonance of such an open cavity system, by varying the acoustic modal response between the parallel barriers. By adding multiple resonators, noise abatement within a wide frequency range can also be achieved. The following specific conclusions can be drawn:

1. A theoretical model, capable of dealing with the acoustical interactions between the Helmholtz resonator and two-dimensional open cavity was developed. The model was demonstrated to be able to characterize the effect of the Helmholtz resonator on the acoustic field of parallel barriers well and can therefore be used as a useful design and analysis tool. With the help of the proposed design for suppression of the acoustic modal response inside the open cavity, single or multiple resonance peaks of the open cavity can be controlled.
2. The performance of the parallel barriers integrated with the Helmholtz resonator is dependent on its mounting location. The optimal location of the HR is no longer traditionally found at any arbitrary point of the anti-nodal surface. It was determined that the resonator should be located close to the primary sound source. With the optimal position of HR281 at approximately (0, -0.85) m, noise reduction around the target frequency can be achieved desirably without enhancement of the sound pressure level in a high frequency range.
3. With the appropriate design of HR, the dominant modal response at the peak frequency of sound pressure level spectrum will be suppressed significantly, which results in the incident sound wave at the barrier top edge being reduced. In addition to the magnitude, incident wave angle will bend slightly towards the parallel direction along the barrier surface; thus, the diffraction wave that propagates from the top edge to the shadow zone will be reduced. Therefore, the use of HRs can suppress the diffraction field at the barrier top.
4. An experimental study was conducted to verify the theoretical model and demonstrate the

feasibility of using Helmholtz resonators integrated into the parallel barriers. Five resonators with the same natural frequency of 281 Hz were used to reduce the sound peak at 289 Hz. Roughly speaking, the measured sound pressure levels of the parallel barriers with and without the resonator reasonably match the predicted data derived from the theoretical model. An average reduction of about 4.36 dB can be achieved in the frequency range of 251 Hz to 295 Hz, which covers the target frequency.

Acknowledgments

The authors would like to acknowledge the funding support from The Research Grants Council of the Hong Kong SAR government (PolyU 5140/13E) and The Hong Kong Polytechnic University (G-YBN2) and (G-YBYA). The first author also thanks the Hong Kong Polytechnic University for the research studentship.

References

[1] D. Hutchins, H. Jones, B. Paterson, L. Russell, Studies of parallel barrier performance by acoustical modeling, J. Acoust. Soc. Am. 77 (1985) 536-546.
[2] C. Yang, J. Pan, L. Cheng, A mechanism study of sound wave-trapping barriers, J. Acoust. Soc. Am. 134 (2013) 1960-1969.
[3] G. Watts, Acoustic performance of parallel traffic noise barriers, Appl. Acoust. 47 (1996) 95-119.
[4] T. Ishizuka, K. Fujiwara, Performance of noise barriers with various edge shapes and acoustical conditions, Appl. Acoust. 65 (2004) 125-141.
[5] D. Crombie, D. Hothersall, The performance of multiple noise barriers, J. Sound Vibr. 176 (1994) 459-473.
[6] D.N. May, N. Osman, Highway noise barriers: new shapes, J. Sound Vibr. 71 (1980) 73-101.
[7] K. Fujiwara, D.C. Hothersall, C.-h. Kim, Noise barriers with reactive surfaces, Appl. Acoust. 53 (1998) 255-272.
[8] M. Monazzam, Y. Lam, Performance of profiled single noise barriers covered with quadratic residue diffusers, Appl. Acoust. 66 (2005) 709-730.
[9] M.R. Monazzam, S.M.B. Fard, Impacts of different median barrier shapes on a roadside environmental noise screen, Environ. Eng. Sci. 28 (2011) 435-441.
[10] J. Pan, R. Ming, J. Guo, Wave trapping barriers, in Proceedings of Acoustics (2004) 283-

288.
[11] X. Wang, D. Mao, W. Yu, Z. Jiang, Sound barriers from materials of inhomogeneous impedance, J. Acoust. Soc. Am. 137 (2015) 3190-3197.
[12] D. Li, L. Cheng, Acoustically coupled model of an enclosure and a Helmholtz resonator array, J. Sound Vibr. 305 (2007) 272-288.
[13] D. Li, L. Cheng, G. Yu, J. Vipperman, Noise control in enclosures: Modeling and experiments with T-shaped acoustic resonators, J. Acoust. Soc. Am. 122 (2007) 2615-2625.
[14] G. Yu, L. Cheng, Location optimization of a long T-shaped acoustic resonator array in noise control of enclosures, J. Sound Vibr. 328 (2009) 42-56.
[15] G. Yu, D. Li, L. Cheng, Effect of internal resistance of a Helmholtz resonator on acoustic energy reduction in enclosures, J. Acoust. Soc. Am. 124 (2008) 3534-3543.
[16] K. Chen, Y. Chen, K. Lin, C. Weng, The improvement on the transmission loss of a duct by adding Helmholtz resonators, Appl. Acoust. 54 (1998) 71-82.
[17] A. Selamet, V. Kothamasu, J. Novak, Insertion loss of a Helmholtz resonator in the intake system of internal combustion engines: an experimental and computational investigation, Appl. Acoust. 62 (2001) 381-409.
[18] S.-H. Seo, Y.-H. Kim, Silencer design by using array resonators for low-frequency band noise reduction, J. Acoust. Soc. Am. 118 (2005) 2332-2338.
[19] S.J. Esteve, M.E. Johnson, Adaptive Helmholtz resonators and passive vibration absorbers for cylinder interior noise control, J. Sound Vibr. 288 (2005) 1105-1130.
[20] S.J. Estéve, M.E. Johnson, Reduction of sound transmission into a circular cylindrical shell using distributed vibration absorbers and Helmholtz resonators, J. Acoust. Soc. Am. 112 (2002) 2840-2848.
[21] C.Q. Howard, C.H. Hansen, A. Zander, Vibro-acoustic noise control treatments for payload bays of launch vehicles: discrete to fuzzy solutions, Appl. Acoust. 66 (2005) 1235-1261.
[22] L.N. Cattafesta, Q. Song, D.R. Williams, C.W. Rowley, F.S. Alvi, Active control of flow-induced cavity oscillations, Prog. Aeosp. Sci. 44 (2008) 479-502.
[23] S. Hein, T. Hohage, W. Koch, On resonances in open systems, J. Fluid Mech. 506 (2004) 255-284.
[24] W. Koch, Acoustic resonances in rectangular open cavities, AIAA J. 43 (2005) 2342-2349.
[25] Y. Tong, Y. Kou, J. Pan, Forced acoustical response of a cavity coupled with a semi-infinite space using coupled mode theory, Wave Motion 73 (2017) 11-23.
[26] F.J. Fahy, Foundations of engineering acoustics, Academic press, 2000.
[27] S. Kim, J. Pasciak, The computation of resonances in open systems using a perfectly matched layer, Math. Comput. 78 (2009) 1375-1398.
[28] J.B. Keller, Geometrical theory of diffraction, J. Opt. Soc. Amer. 52 (1962) 116-130.
[29] K. Li, M. Law, M. Kwok, Absorbent parallel noise barriers in urban environments, J. Sound Vibr. 315 (2008) 239-257.

Figure Captions

Fig. 1. A schematic diagram of the parallel barriers integrated with multiple Helmholtz resonators.

Fig. 2. Sketch of the integration surface used in Eq.(7) for parallel barrier.

Fig. 3. Comparison among the present theoretical model, boundary element method (BEM) and method of superposition of trapped modes for prediction of sound pressure level.

Fig. 4. Comparison of SPLs at different receiving points for the parallel barriers with and without HR281. (a) receiver at (5, -0.9) m; (b) receiver at (5, 0) m; (c) receiver at (10, -0.9) m and (d) receiver at (10, 0) m.

Fig. 5. The SPL distributions between parallel barriers with the sound source at (0.1, -0.9) m for the frequency (a) f =109 Hz; (b) f =198 Hz; (c) f =289 Hz; (d) f =381 Hz; (e) f =474 Hz; (f) f =567 Hz; (g) f =660 Hz; (h) f =753 Hz and (i) f =940 Hz.

Fig. 6. Comparison of amplitudes of the enclosed cavity mode and external mode for the parallel barriers with and without HR281. (1a) $|a_j|$ for 289 Hz (1b) $|b_m|$ for 289Hz, (2a) $|a_j|$ for 847Hz and (2b) $|b_m|$ for 847 Hz.

Fig. 7. The sound pressure distributions for the parallel barriers with and without HR281: (1a) and (1b) without the resonator for f=289Hz and f=847Hz respectively; (2a) and (2b) with HR281 for f=289Hz and f=847Hz respectively.

Fig. 8. Variation of SPL spectrum when HR281 at different positions.

Fig. 9. Optimization curve of IL_{mean} for different mounting locations of the HR281. (a) HR281 is mounted on the left-hand side of parallel barriers and (b) HR281 is mounted on the right-hand side of parallel barriers.

Fig. 10. Comparison of sound intensity distributions of the parallel barriers with and without HR281 at 289 Hz: (a) without the resonator and (b) with the HR281 at (0, -0.9) m.

Fig. 11. Comparison of SPL for parallel barriers with and without two Helmholtz resonator models at different positions.

Fig. 12. Sound response measurement system. (a) Experimental set-up and (b) photo.

Fig. 13. Experimental results of SPL for the parallel barriers with and without HR281.

Table 1. The comparison of the eigenvalues of the first ten (m, 0) enclosed cavity modes and the frequencies of the sound pressure level for a parallel barriers.